Empowering the Bandwidth of Continuous Mode Symmetrical Doherty Amplifiers by Leveraging on Fuzzy Logic Techniques

Gideon Naah, *Student Member, IEEE,* and Rocco Giofrè, *Senior Member, IEEE*

***Abstract*—Achieving a fractional bandwidth (FBW) of more than 60% has been a challenging problem for two-way symmetrical Doherty power amplifiers (TW-SDPAs) that are designed using continuous mode technique. As reported in the literature, these designed continuous mode-based TW-SDPAs possess less than 52% FBW which cannot satisfactorily meet the challenging, complex and ever-evolving modulation schemes' demands. To overcome such a limitation, this paper proposes a novel approach based on fuzzy logic techniques able to simplify and to speed up the design of continuous mode-based TW-SDPAs with state-of-art FBW. In particular, the proposed technique uses K-means unsupervised learning clustering algorithm and continuous mode technique in a modelled fuzzy logic system environment. As a result, extensive impedance solution design space is readily made available and the optimal impedances required by the carrier and peaking sub-amplifiers for efficiently operating at the saturation and output-power-back-off (OPBO) levels are automatically obtained. For verification, a TW-SDPA was designed and measured. According to the measured results, the TW-SDPA operates within 1.2−2.4 GHz frequency band, corresponding to 66.7% FBW. As compared to the designed continuous mode-based TW-SDPAs reported in the literature, this work indicates over 15% increment in FBW. Moreover, 41.59%−81.1% drain efficiency (DE) at saturation, 35%−63% DE at 6 dB OPBO, 42−45 dBm output power and 7−10.52 dB gain were successfully achieved. Adjacent channel leakage ratio (ACLR) better than −46 dBc and average DE within 46%−55% were successfully recorded after linearisation.**

***Index Terms*—Continuous mode, Doherty power amplifiers (DPAs), fuzzy logic technique, fractional bandwidth (FBW).**

I. Introduction

DUE to the complex and ever-evolving nature of modulation schemes in wireless communication systems, power amplifiers (PAs) with large fractional bandwidth (FBW) and high-efficiency capabilities are in high demand. For that reason, radio frequency (RF) and microwave PA researchers have been pushed beyond the conventional limits and methods for designing PAs in order to meet the current and future needs. For instance, energy harvesting techniques have been introduced in PA designs in order to further improve the performance [1]–[3].

Manuscript received XXXX XX, XXXX; revised XXXX XX, XXXX; accepted XXXX XX, XXXX. Date of publication XXXX XX, XXXX; date of current version XXXX XX, XXXX.

The authors are with the Electronics Engineering Department, University of Rome Tor Vergata, 00133, Rome, Italy (e-mail: engrgnaah7@gmail.com; giofr@ing.uniroma2.it).

Color versions of one or more of the figures in this letter are available online at http://ieeexplore.ieee.org.

Digital Object Identifier XX.XXXX/TMTT.2019.XXXXXXX

Furthermore, diverse fuzzy logic techniques such as interval type-2 fuzzy inference engine [4], self-organising fuzzy neural networks (SOFNNs) [5], radial-basis function neural networks (RBFNNs) [6], adaptive neuro-fuzzy inference system (ANFIS)-based Hammerstein [7], modified adaptive neuro-fuzzy inference system (MANFIS) [8] and many others [9]–[14] have been used by RF and microwave researchers to adequately solve the linearisation problems as well as reducing the power consumption level in PAs. Although the linearity performance in the reported amplifiers are substantially improved using these fuzzy logic techniques, the FBW performance of the amplifiers were not considered. The PAs were designed to function at single frequency points. This could be attributed to the motivation behind the designs and that is, enhancing the linearity performance in amplifiers.

Fifth-generation (5G) technology is the next-generation wireless technology being worked on by the industry and academia. It is expected to provide a data rate of 10-50 Gbps [16]. Despite its expected high functionalities, the large signal bandwidth required for high-speed data transmission is limited by the scarce spectrum resources. This therefore imposes stringent bandwidth requirements on the PAs.

Varieties of techniques and architectures that are based on the Doherty operating principle have been proposed for bandwidth extension [15]–[45]. Some of these techniques are the real frequency technique [21], Bayesian optimisation technique [31] and continuous mode technique [32–36]. Sun and Jansen [21] proposed the design of two-way symmetrical Doherty power amplifiers (TW-SDPAs) using real frequency technique. However, the recorded FBW is less than 30%. Similarly, Chen *et al.* [31] also proposed Bayesian optimisation for designing the TW-SDPAs. Nevertheless, the measured FBW is less than 47%. In the case of the continuous mode TW-SDPAs proposed by Chen *et al.* [32–34] and Shi *et al.* [35–36], the reported bandwidths are also less than 52% even if the beneficial effect of the continuous mode technique on the efficiency figure was tangible. Giofrè *et al.* [40], Yang *et al.* [42] and Rubio *et al.* [43] proposed TW-SDPAs that were not accomplished using continuous mode technique. Upon comparing [40], [42] and [43] with [32–36], this is a clear indication that the reported continuous mode-based TW-SDPAs are critically facing bandwidth problems. As a result, cannot meet the challenging demands and the successful deployment of modern wireless communication systems. In summary, none of the continuous mode TW-SDPA designs reported in the literature have considered a modelled fuzzy

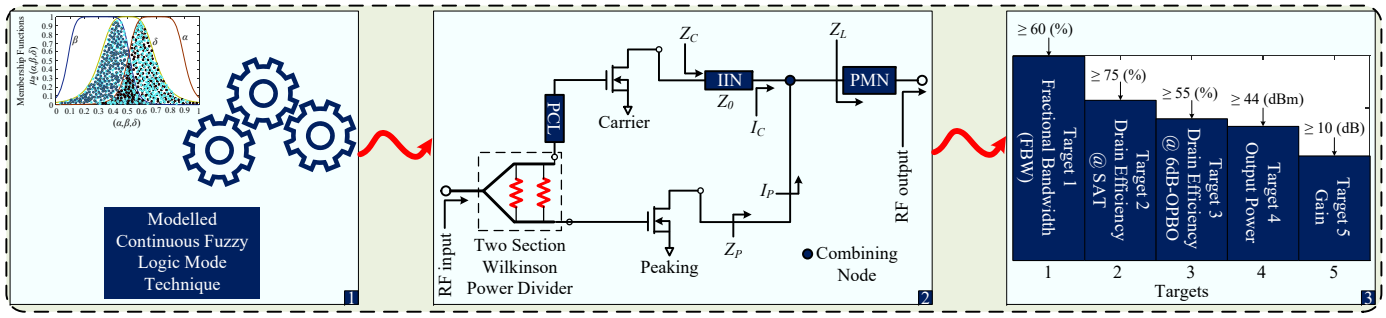

(a) (b) (c)

Fig. 1. Simplified conceptual framework of the proposed two-way symmetrical DPA design steps. (a) Proposed continuous fuzzy logic mode technique to be applied in designing the two-way symmetrical DPA. (b) Proposed two-way symmetrical DPA architecture. (c) Expected performance indicators from the two-way symmetrical DPA. Note: SAT and OPBO, respectively, designate saturation and output-power-back-off.

logic and continuous mode techniques with K-means unsupervised learning clustering algorithm for solving the bandwidth problem in the continuous mode TW-SDPAs.

To address the bandwidth limitations in the continuous mode-based TW-SDPAs, a continuous fuzzy logic mode technique (CFLMT) is proposed in this paper. The proposed technique uses a modelled K-means unsupervised learning clustering algorithm and a modelled continuous mode technique in a modelled fuzzy logic system environment which can extend the bandwidth of the TW-SDPA. To extend the bandwidth of the TW-SDPA, the proposed methodology directly solves for the TW-SDPA design parameters in two separate sub-clustered regions. The optimal impedances required by the carrier and peaking sub-amplifiers for efficiently operating at the saturation and output-power-back-off (OPBO) levels are automatically obtained. Even though the major target in this paper is to solve the bandwidth problem in the continuous mode-based TW-SDPAs, substantial performance indicators such as efficiency, output power and gain were not ignored. For validating the proposed technique, a 1.2–2.4 GHz TW-SDPA with 66.7% FBW was designed, implemented and measured. Upon comparing the FBW performance of the proposed TW-SDPA to that reported by Chen *et al.* [32–34] and Shi *et al.* [35–36], 15.5%–29.7% increment in FBW is successfully demonstrated by the proposed TW-SDPA in this work.

The residue of this paper is organised as follows: Section II presents the analysis of the proposed TW-SDPA concept. Section III gives the design approach for the proposed broadband TW-SDPA. Measurement results under different excitations of the continuous wave and the modulated signals are given in Section IV. Conclusions are finally presented in Section V.

II. Proposed Two-Way Symmetrical DPA Concept

The simplified conceptual framework of the proposed TW-SDPA design steps is shown in Fig. 1. The modelled CFLMT for designing the TW-SDPA is shown in Fig. 1(a), where α, δ and β pertain to the CFLMT membership function parameters with their associated shapes shown from right to left, respectively. Moreover, the granules shown are training nodes to be used in acquiring the optimal impedances for effective load modulation in the TW-SDPA operation. The proposed TW-SDPA architecture is shown in Fig. 1(b), where Z_C and Z_P represent the load impedances, at the device output, of the carrier and peaking amplifiers while I_C and I_P are the correspondent currents, respectively. Z_0 designates the characteristic impedance of the impedance inverting network (IIN). The TW-SDPA consists of a carrier PA and a peaking PA for which they are independently biased in class-B and class-C, respectively. These two sub-amplifiers are combined by a two-section Wilkinson power divider at the input and connected to a common load Z_L at the output. A post-matching network (PMN) is therefore constructed for matching the standard 50 Ω to Z_L at the combining node. The PMN provides an appropriate fundamental load termination. The architecture is then completed with the phase compensation line (PCL). Targets 1–5 in Fig. 1(c) indicate the levels of priorities assigned to the expected performance indicators from the TW-SDPA to be designed. Target 1 indicates the topmost prioritised goal followed by Target 2 being the second most prioritised goal. Then to the third, fourth and finally, to the fifth prioritised goal. Clearly, both the targets and their order are not fixed and can be chosen in accordance with the designer needs.

According to the existing TW-SDPA concept on active load modulation, the effective load impedances of the carrier and peaking branches at the combining node can be expressed as

$$\begin{cases} Z_{C@OPBO} = \left(\dfrac{Z_0^2}{\left(1+\frac{I_{P@Sat}}{I_{C@Sat}}\right) Z_L} \right) \\ Z_{C@Sat} = \left(1 + \frac{I_{P@Sat}}{I_{C@Sat}}\right) Z_L \end{cases} \tag{1}$$

$$\begin{cases} Z_{P@OPBO} = \infty \\ Z_{P@Sat} = \left(1 + \frac{I_{C@Sat}}{I_{P@Sat}}\right) Z_L. \end{cases} \tag{2}$$

where $Z_{C@Sat}$ and $Z_{P@Sat}$ represent the load impedances, at the device output, of the carrier and peaking amplifiers at saturation while $Z_{C@OPBO}$ and $Z_{P@OPBO}$ are the load impedances at OPBO, respectively. $I_{C@Sat}$ and $I_{P@Sat}$ are currents pertaining to the carrier and peaking amplifiers at saturation, respectively.

Assuming that the TW-SDPA to be accomplished satisfies the normalised continuous mode voltage waveform condition given in the following relation which is deduced from [46]

$$v_{ds}(t) = (1 - (\alpha \cos(\omega t) - \delta \cos(3\omega t))\beta)(1 - \gamma \sin(\omega t)) \tag{3}$$

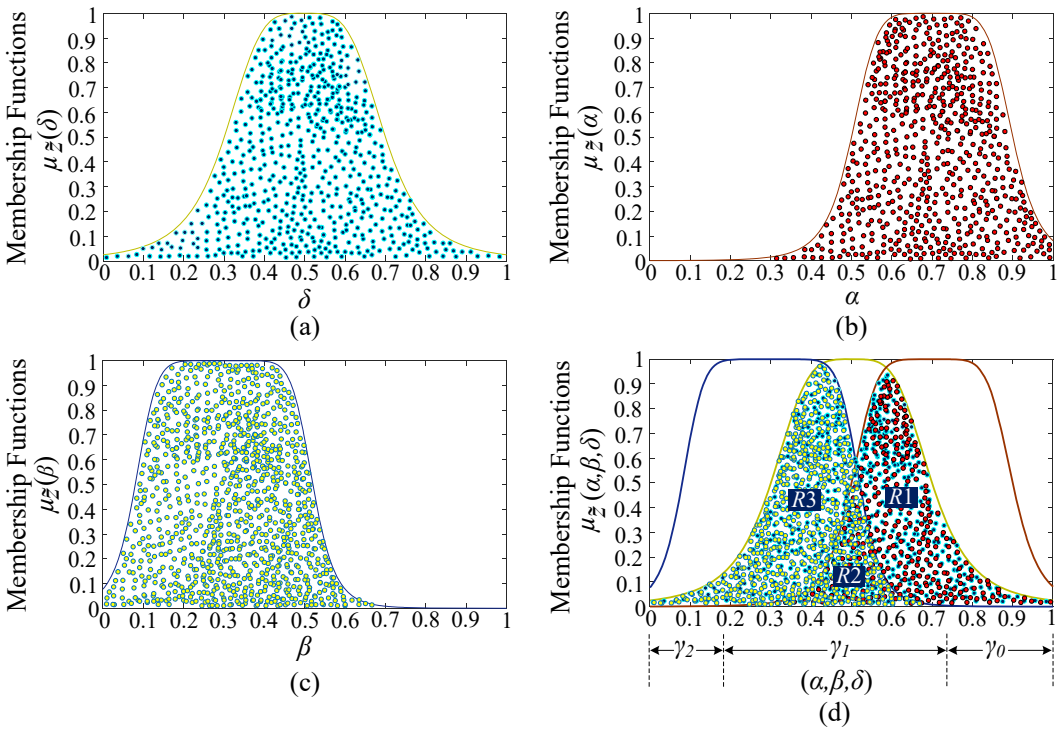

Fig. 2. Continuous fuzzy logic modes membership functions. (a) δ membership function. (b) α membership function. (c) β membership function. (d) α, δ and β continuous fuzzy logic modes membership functions. Note: $R1$, $R2$ and $R3$ in (d) denote regions 1, 2 and 3, respectively.

where α, β, δ and γ designate the continuous fuzzy logic mode parameters to be used in obtaining the optimum characteristic impedances and electrical lengths of the transmission lines in the TW-SDPA, and load impedances required by the carrier and peaking devices for efficiently operating at the saturation and OPBO levels. To effectively characterise the CFLMT operating conditions, the γ parameter has been specified to function within 0 and 1, i.e. $0 \leq \gamma \leq 1$. This differs from the conventional continuous mode operating condition where γ ranges from -1 to 1, i.e. $-1 \leq \gamma \leq 1$. The reason for specifying the γ parameter to function within 0 and 1 is to satisfy the membership function conditions in the fuzzy logic system as proposed by Zadeh [47].

A. Modelling of the Continuous Fuzzy Logic Mode Membership Functions

Shown in Fig. 2 is the continuous fuzzy logic mode membership functions under normalised conditions. Supposing that there exists a universe of discourse Z and its elements are designated by δ, α and β, then a fuzzy set $\tilde{z}$ in Z can be expressed as

$$\tilde{z} = \left\{(\alpha, \beta, \delta), \mu_{\tilde{z}(\alpha,\beta,\delta)} | (\alpha, \beta, \delta) \in Z\right\} \tag{4}$$

where $\mu_{\tilde{z}(\delta)}$, $\mu_{\tilde{z}(\alpha)}$ and $\mu_{\tilde{z}(\beta)}$ are defined as the membership functions (see Figs. 2(a)–(c)). Collectively, the membership functions can be defined as $\mu_{\tilde{z}(\alpha,\beta,\delta)}$ (see Fig. 2(d)). The CFLMT proposed in this work uses K-means unsupervised learning clustering algorithm. For that matter, data nodes are needed in the training. As clearly demonstrated in Fig. 2, within each sub-figure lies a set of nodes for which will help determine the suitable impedances and electrical lengths for designing the TW-SDPA. In Fig. 2(d), $R1$, $R2$ and $R3$, respectively, signify regions 1, 2 and 3. By unifying Fig. 2(a), Fig. 2(b) and Fig. 2(c), Fig. 2(d) is obtained as a consequence. Since each sub-figure contains training data nodes, it will be appropriate to present them in a unified setting, then find the optimum nodes within each region. As illustrated in Figs. 2(a)–(c), the nodes in Fig. 2(a) cannot be found in Figs. 2(b) and (c), and vice versa. However, in Fig. 2(d), all the training nodes can be found in $R1 \sim R3$. By this approach, a reduced number of fuzzy rules and parameters can be guaranteed and as a consequence, can lead to obtaining better convergence solutions. Furthermore, the time-wasting search carried out by most algorithms, which even leads to convergence problems, can be avoided.

In reference to Fig. 2(d), by applying fuzzy sets theory, the α, δ and β parameters are bounded to function within $0 \leq \alpha \leq 1$, $0 \leq \delta \leq 1$ and $0 \leq \beta \leq 0.5$, respectively. The constraint placed on the β parameter clearly indicates that even though it influences the α and δ parameters, the highest priorities are placed on the α and δ parameters. This is because, the α and δ parameters strongly determine and guarantee the CFLMT operating conditions. Moreover, considering Fig. 2(d), the optimal training nodes associated to the α, δ and β parameters to be determined in $R1 \sim R3$, can be specified in a data solution space for which it is defined as continuous fuzzy mode solution space (CFMSS). In order to determine the CFMSS in $R1$ where the optimal training nodes associated to the α and δ parameters can be found, the relation below can be applied

$$CFMSS_{R1} = jR1 \int_{\gamma_{0,x=0.73}}^{\gamma_{0,y=1}} \alpha_i(\tilde{z})\delta_i(\tilde{z})\, d\tilde{z} \tag{5}$$

where $jR1$ indicates the total number of nodes, i.e. j in $R1$, $i = 1, 2, 3, ..., nth$, and $\gamma_{0,x}$ and $\gamma_{0,y}$, respectively, designate the lower and upper limit membership function boundary conditions for α and δ in $R1$. Similarly, to determine the CFMSS in $R2$ and $R3$, the relations below can be applied

$$CFMSS_{R2} = kR2 \int_{\gamma_{1,x=0.18}}^{\gamma_{1,y=0.73}} \alpha_i(\tilde{z})\delta_i(\tilde{z})\beta_i(\tilde{z})\ d\tilde{z} \tag{6}$$

$$CFMSS_{R3} = lR3 \int_{\gamma_{2,x=0}}^{\gamma_{2,y=0.18}} \delta_i(\tilde{z})\beta_i(\tilde{z})\ d\tilde{z} \tag{7}$$

where $kR2$ and $lR3$ indicate the total number of nodes, i.e. k and l in $R2$ and $R3$, respectively, $i = 1, 2, 3, ..., nth$, $\gamma_{1,x}$ and $\gamma_{1,y}$, and $\gamma_{2,x}$ and $\gamma_{2,y}$, respectively, designate the lower and upper limit membership function boundary conditions for α, δ and β parameters in $R2$, and δ and β parameters in $R3$. With the introduced γ_0, γ_1 and γ_2 lower and upper limit membership functions boundary conditions in $R1$, $R2$ and $R3$, respectively, the effect of high levels of uncertainties in the CFLMT can be better handled and minimised. By taking into consideration $R1$, $R2$ and $R3$, the overall CFMSS can be expressed as

$$\begin{aligned} CFMSS_T = \ & jR1 \int_{\gamma_{0,x=0.73}}^{\gamma_{0,y=1}} \alpha_i(\tilde{z})\delta_i(\tilde{z})\ d\tilde{z} + \\ & kR2 \int_{\gamma_{1,x=0.18}}^{\gamma_{1,y=0.73}} \alpha_i(\tilde{z})\delta_i(\tilde{z})\beta_i(\tilde{z})\ d\tilde{z} + \\ & lR3 \int_{\gamma_{2,x=0}}^{\gamma_{2,y=0.18}} \delta_i(\tilde{z})\beta_i(\tilde{z})\ d\tilde{z}. \end{aligned} \tag{8}$$

Appropriate load modulating conditions in (1)–(2) for the conventional continuous mode-based TW-SDPAs cannot be exactly accomplished over a continuous frequency range due to the well-known matching limitations [48]. Therefore, by introducing (8) in (1) and (2), the CFLMT may find the optimum impedances required by the carrier and peaking sub-amplifiers for effective load matching and load modulating conditions at both saturation and OPBO levels, as a consequence, providing bandwidth extension and high-efficiency enhancement. That said, the relations for (1) and (2) may be, respectively, redefined as follows after some rearrangement

$$\begin{cases} Z_{C@OPBO} = Z_0^2 / \Big(jR1 \int_{\gamma_{0,x=0.73}}^{\gamma_{0,y=1}} \alpha_i(\tilde{z})\delta_i(\tilde{z})\ d\tilde{z} + \\ \qquad kR2 \int_{\gamma_{1,x=0.18}}^{\gamma_{1,y=0.73}} \alpha_i(\tilde{z})\delta_i(\tilde{z})\beta_i(\tilde{z})\ d\tilde{z} + \\ \qquad lR3 \int_{\gamma_{2,x=0}}^{\gamma_{2,y=0.18}} \delta_i(\tilde{z})\beta_i(\tilde{z})\ d\tilde{z} + \frac{I_{P@Sat}}{I_{C@Sat}} \Big) Z_L \\ Z_{C@Sat} = \Big(jR1 \int_{\gamma_{0,x=0.73}}^{\gamma_{0,y=1}} \alpha_i(\tilde{z})\delta_i(\tilde{z})\ d\tilde{z} + \\ \qquad kR2 \int_{\gamma_{1,x=0.18}}^{\gamma_{1,y=0.73}} \alpha_i(\tilde{z})\delta_i(\tilde{z})\beta_i(\tilde{z})\ d\tilde{z} + \\ \qquad lR3 \int_{\gamma_{2,x=0}}^{\gamma_{2,y=0.18}} \delta_i(\tilde{z})\beta_i(\tilde{z})\ d\tilde{z} + \frac{I_{P@Sat}}{I_{C@Sat}} \Big) Z_L \end{cases} \tag{9}$$

$$\begin{cases} Z_{P@OPBO} = \infty \\ Z_{P@Sat} = \Big(jR1 \int_{\gamma_{0,x=0.73}}^{\gamma_{0,y=1}} \alpha_i(\tilde{z})\delta_i(\tilde{z})\ d\tilde{z} + \\ \qquad kR2 \int_{\gamma_{1,x=0.18}}^{\gamma_{1,y=0.73}} \alpha_i(\tilde{z})\delta_i(\tilde{z})\beta_i(\tilde{z})\ d\tilde{z} + \\ \qquad lR3 \int_{\gamma_{2,x=0}}^{\gamma_{2,y=0.18}} \delta_i(\tilde{z})\beta_i(\tilde{z})\ d\tilde{z} + \frac{I_{C@Sat}}{I_{P@Sat}} \Big) Z_L. \end{cases} \tag{10}$$

B. Modelling of the Continuous Fuzzy Mode Impedance Solution Design Space

Supposing that the fundamental (Z_{CFM1}) and second (Z_{CFM2}) harmonic impedance domain relating to the continuous fuzzy logic mode from which the suitable OPBO and saturation impedances, characteristic impedance and electrical length of each transmission line of the TW-SDPA may be obtained, Z_{CFM1} and Z_{CFM2} are, respectively, expressed as

$$\begin{aligned} Z_{CFM1} = \ & Z_{\Re} \Bigg(\Bigg(\alpha\delta + \alpha \Bigg(\frac{1+\beta}{2} \Bigg) - \beta\gamma \Bigg) + \\ & j \Bigg(\delta \Bigg(1 - \beta \Bigg) \gamma - \sin\gamma \Bigg) \Bigg) \end{aligned} \tag{11a}$$

$$Z_{CFM2} = Z_{\Re} + j \Bigg(\alpha\delta \Bigg(- \Bigg(\Bigg(1 - \beta \Bigg) \frac{3\pi}{8} \gamma \Bigg) \Bigg) \Bigg) \tag{11b}$$

$$Z_{CFM3} = \infty \tag{11c}$$

where $Z_{\Re}$ = (9) and (10) ($Z_{P@OPBO} = \infty$ is omitted in (11) since the peaking PA is off). With (11a) and (11b), the suitable harmonic load impedances are obtained and kept away from the open-circuited region in the Smith chart where the performance of continuous mode-based TW-SDPAs deteriorates. Moreover, with (9) and (10) introduced in (11), (11) influences the load modulation and load matching conditions in the output matching newtorks (OMNs), IIN and PMN of the TW-SDPA. As a consequence, this can lead to bandwidth extension and high-efficiency OPBO operation.

C. Modelling of the K-Means Unsupervised Learning Clustering Algorithm for the Continuous Fuzzy Mode Impedance Solution Design Space

First and foremost, it is essential to note that most algorithms used in the TW-SDPA designs do function with high number of variables, rules and techniques. By these approaches, it is very difficult to tell which variable belongs to which sub-amplifier for saturation and OPBO operations. In order to solve this kind of problem and to make the design process more easier for the RF/microwave PA designer, the proposed technique rather feeds-in the modelled CFM equations into the proposed system. It is evident that the number of variables in the modelled CFM equations are two to be precise, thus α and δ. Only that the influence of the β variable is considered which makes it appear to have only three variables in all. Moreover, for each modelled CFM equation, one can easily determine the required optimal variables with their associated impedance values belonging to each sub-amplifier for saturation and OPBO operations.

In the K-means unsupervised learning clustering algorithm, there are four K clusters in all which are associated to the performance indicators with the five targets shown in Fig. 1(c). Each K cluster possesses two sub-clusters labelled as $R1$ and $R2$. More than 700 training nodes are assigned to each sub-cluster. Moreover, no initial guesses are required [31]. Furthermore, according to the continuous mode operation technique, the third harmonic impedance, thus Z_{CFM3} must be equated to ∞. For that matter, Z_{CFM3} is void of training

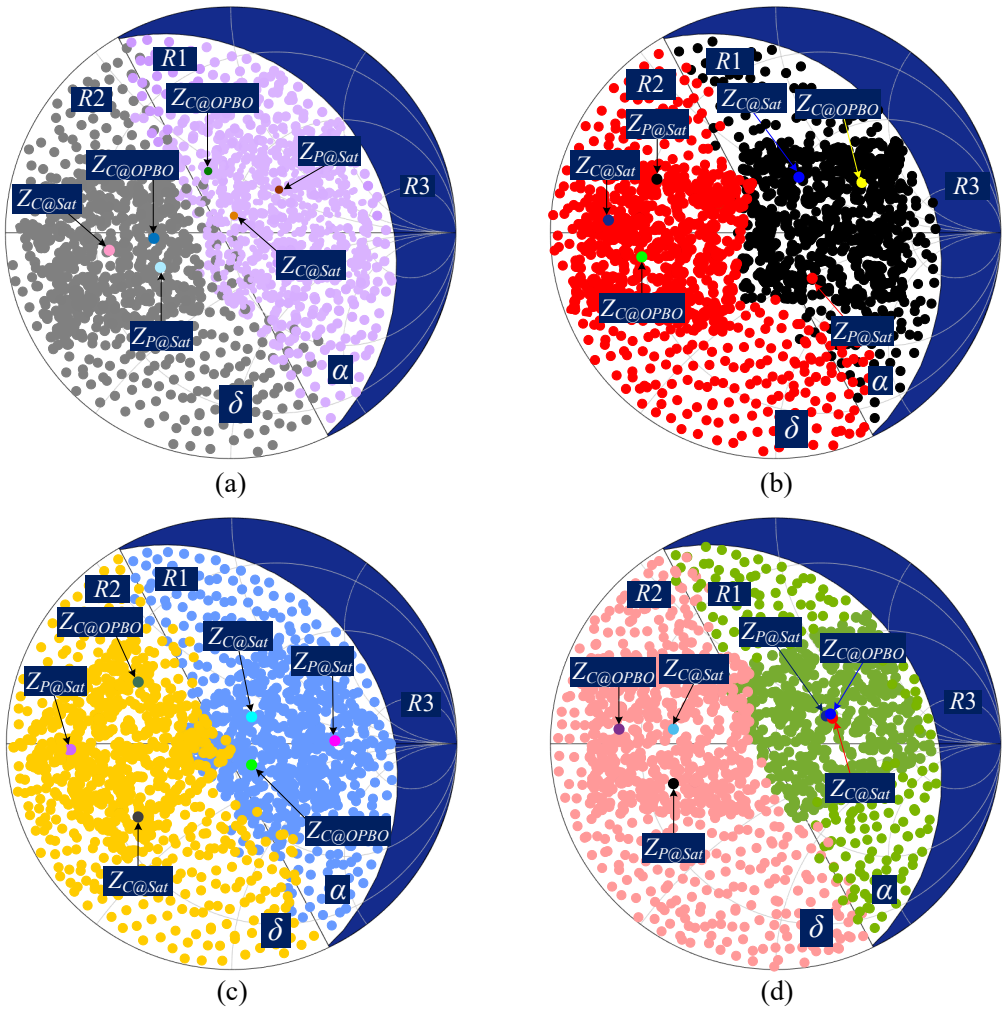

Fig. 3. Continuous fuzzy logic modes K-means unsupervised learning clustering algorithm demonstration at TW-SDPA's saturation and 6 dB OPBO operations. (a) K_1 cluster–bandwidth impedance solution design space. (b) K_2 cluster–efficiency impedance solution design space. (c) K_3 cluster–output power impedance solution design space. (d) K_4 cluster–gain impedance solution design space.

nodes. This is done to ensure the continuous mode operation condition is satisfied. Also, in order to easily identify the α and δ variables in $R1$ and $R2$, and to lesson computational complexity as well as increase the possibility of finding the optimal convergence solution in the K-means algorithm, α is assigned to $R1$ while δ is assigned to $R2$. Before the formation of each cluster, a centroid also know as mean is selected from the training nodes in each region. The selected centroids move around and the minimum distance between the chosen centroids and other training nodes are calculated. The node with the minimum distance is selected as the new centroid. This process continuous until the cluster centroids stop changing their positions and become static. Once the clusters become static, the K-means clustering algorithm is said to have converged. Finally, the K-means clustering algorithm divides the training nodes into four major clusters with each cluster having two sub-clusters. The objective functions for the K-means algorithm are as follows

$$F_{obj,1} = \sum_{i=1}^{mR1} \sum_{j=1}^{nR2} \left(Z_{C@OPBO} - \mu_{\tilde{z}(\alpha_i,\delta_i)} Z_{opt} \right) \tag{12}$$

$$F_{obj,2} = \sum_{i=1}^{mR1} \sum_{j=1}^{nR2} \left(Z_{C@Sat} - \mu_{\tilde{z}(\alpha_i,\delta_i)} Z_{opt} \right) \tag{13}$$

$$F_{obj,3} = \sum_{i=1}^{mR1} \sum_{j=1}^{nR2} \left(Z_{P@Sat} - \mu_{\tilde{z}(\alpha_i,\delta_i)} Z_{opt} \right) \tag{14}$$

where $mR1$ and $nR2$ designate the total number of selected optimal nodes, i.e. m and n in $R1$ and $R2$, respectively, from $K1 \sim K4$ clusters, and Z_{opt} is the optimal impedance required by a class-B biased CGH40010F transistor. The fuzzy logic system environment suitable for the effective execution of the K-means algorithm comprises three main parts which are (a) fuzzification, (b) fuzzy inference engine with fuzzy rule base and (c) defuzzification. At the fuzzification stage, the modelled CFM equations supplied to the fuzzy system are converted to a suitable form ready for processing. The converted CFM equations are then processed by the fuzzy inference engine. However, the fuzzy inference engine operates strictly based on the fuzzy rules located in the fuzzy rule base. As a matter of fact, the fuzzy rules greatly impact the output to be generated at the defuzzification stage. The defuzzification stage processes the final output. The fuzzy rules employed

in the algorithm are based on IF-THEN rules and are shown below

Rule 1: IF α_i in $R1$ is $\mu_{\alpha_i(\tilde{z})}$, THEN $G = \int_{\gamma_{0,1,x=0.18}}^{\gamma_{0,1,y=1}} \alpha_i(\tilde{z})\, d\tilde{z}$

Rule 2: IF δ_i in $R2$ is $\mu_{\delta_i(\tilde{z})}$, THEN $H = \int_{\gamma_{0,1,2,x=0}}^{\gamma_{0,1,2,y=1}} \delta_i(\tilde{z})\, d\tilde{z}$

where G and H are defined as the consequent parameters, in other words output parameters of the fuzzy system.

After convergence, the optimal α and δ variables in $R1$ and $R2$, respectively, are selected from each K cluster. Otherwise, the fuzzy rules are modified and the process is repeated. The chosen optimal variables associated to each sub-amplifier at both saturation and OPBO operations are then used in designing the TW-SDPA. The performance indicators of the designed TW-SDPA are then verified by simulation in Keysight's Advanced Design System (ADS).

As observed from the K-means algorithm, the reduced number of fuzzy rules and parameters may lead to the acquisition of better convergence results. With the CFM technique, the solution space is limited to $R1$ and $R2$ within the Smith chart. As a result, the time required to find the optimum parameters for the TW-SDPA design is much smaller as compared to the time required in finding the optimum parameters in the entire regions in the Smith chart. Fig. 3 shows the obtained K-means clusters. It is to be noted that Z_{CFM1}, Z_{CFM2} and Z_{CFM3} in (11a), (11b) and (11c) are assigned to $R1$, $R2$ and $R3$, respectively, in each cluster.

Finally, after determining the optimal α and δ parameters in $R1$ and $R2$, respectively, in each K cluster, they are then assigned to their associated impedances of the carrier and peaking sub-amplifiers. In other words, the chosen optimal α and δ parameters in each sub-cluster are assigned to $Z_{C@OPBO}$, $Z_{C@Sat}$ and $Z_{P@Sat}$ for effective load matching and load modulating operation at both saturation and OPBO as shown in Fig. 3. In the case of determining the characteristic impedances (Z_n) and electrical lengths (θ_n) of the transmission lines of the TW-SDPA, similar procedure is used. However, the chosen optimal α and δ parameters are assigned to Z_n and θ_n in each region. This assignment process uses a modelled fuzzy logic max operator for the α and δ parameters for which will be explained in details in Section III. Moreover, it is obvious this design approach not only includes efficiency and output power performance indicators with their associated harmonic load impedances at the initial design stage. Additionally, gain and bandwidth performance indicators are also considered.

III. Proposed Broadband Two-Way Symmetrical DPA Design and Simulation

To commence with the derivation of the actual impedances to be used in designing the TW-SDPA prototype, it is befitting to introduce its design requirements, complete block diagram and complete schematic as shown in Table I, Fig. 4 and Fig. 5, respectively. The design employs two Wolfspeed's CGH40010F gallium nitride (GaN) packaged transistors. The carrier and peaking devices possess a single drain bias voltage supply for which it is set to 28 V while the carrier and peaking gate bias voltages are set to –2.7 V and –5.8 V, respectively. The theory presented in the previous section will be applied to design the TW-SDPA with extended bandwidth and high-efficiency operation in this section. That said, it is vital to

TABLE I
TW-SDPA Design Requirements

Requirement	Symbol	Value	Unit
Fractional Bandwidth	FBW	≥60	%
Output Power Back-Off	OPBO	6	dB
Saturated Drain Efficiency	η_{sat}	≥75	%
OPBO Drain Efficiency	η_{6dB}	≥55	%
Saturated Output Power	Pout	≥44	dBm
Saturated Gain	Gain	≥10	dB

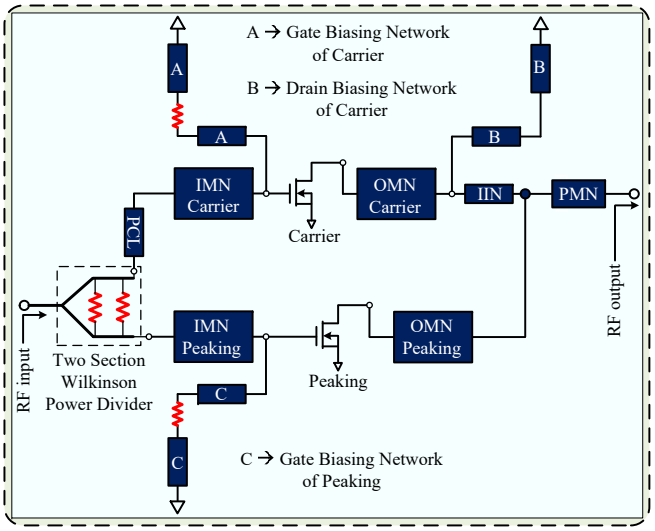

Fig. 4. Complete block diagram of the proposed TW-SDPA.

firstly present the practical DPA circuit design guidelines before giving a demonstration, which are given as follows.

A fuzzy DPA topology with its associated OMNs, input matching networks (IMNs), gate and drain biasing networks, IIN and PMN must firstly be chosen by the designer. Equal number of training data nodes must be set for each sub-cluster. With the fuzzy rules and (12-14) in place, $G = \alpha$ and $H = \delta$ where α and δ signify the optimal parameters to be obtained from the sub-clusters at the defuzzification stage. With (12-14), the degree of mismatch within the chosen fuzzy DPA topology can be minimised. Moreover, acquiring better convergence solutions can be made possible. This can lead to better transition from the fuzzy DPA topology to the actual DPA topology realisation. Then, execute the proposed algorithm in order to obtain the optimal α and δ parameters from each K cluster. After convergence, from (11a)-(11b), (9) and (10) relating to the carrier and peaking PAs, respectively, are firstly determined.

Next, to determine the characteristic impedance and electrical length for all the transmission lines in each chosen network such as OMN, first replace (9) and (10) in (11) with Z_n and θ_n where $n = 1, 2, 3, \ldots$ Furthermore, to use Z_n and θ_n in the objective functions, Z_n replaces $Z_{C@Sat}$ in (13) while θ_n replaces $Z_{P@Sat}$ in (14). For θ_n in (14), Z_{opt} is replaced by θ_{opt} where θ_{opt} defines the optimum electrical length of the transmission lines. Execute the algorithm once again to obtain the optimal α and δ parameters from each K cluster after convergence. That means, to determine the optimal α and δ

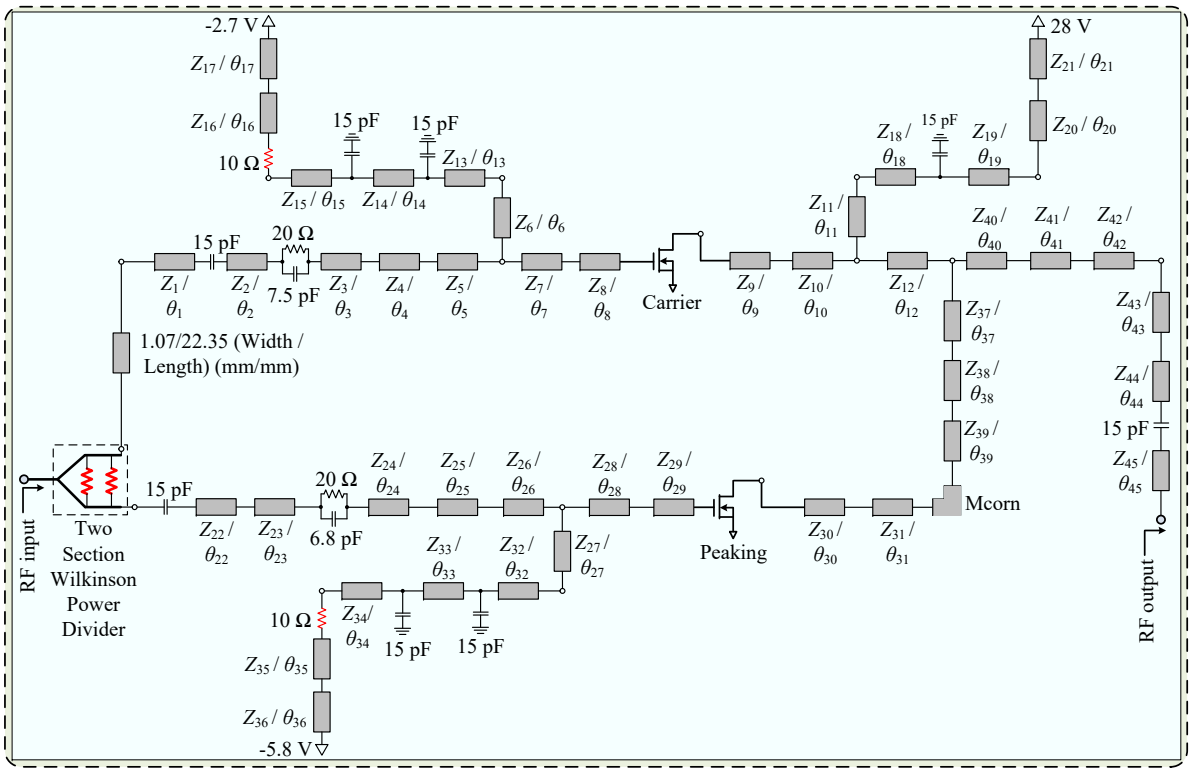

Fig. 5. Complete schematic of the proposed TW-SDPA. The impedance and electrical length design values of the TW-SDPA are given in Table IV.

TABLE II
OPTIMAL α AND δ PARAMETERS OBTAINED FOR $Z_{C@OPBO}$, $Z_{C@Sat}$ AND $Z_{P@Sat}$ FROM $R1 \sim R2$ IN $K1 \sim K4$ CLUSTERS AFTER CONVERGENCE

α Parameters Obtained From $R1$ in $K1 \sim K4$ Clusters			
$K1(R1)$	$K2(R1)$	$K3(R1)$	$K4(R1)$
$\alpha_0 = 0.5 = Z_{C@OPBO}$	$\alpha_1 = 0.1 = Z_{C@OPBO}$	$\alpha_2 = 0.3 = Z_{C@OPBO}$	$\alpha_3 = 0.7 = Z_{C@OPBO}$
$\alpha_4 = 0.95 = Z_{C@Sat}$	$\alpha_5 = 0.83 = Z_{C@Sat}$	$\alpha_6 = 0.6 = Z_{C@Sat}$	$\alpha_7 = 0.2 = Z_{C@Sat}$
$\alpha_8 = 0.71 = Z_{P@Sat}$	$\alpha_9 = 0.15 = Z_{P@Sat}$	$\alpha_{10} = 1 = Z_{P@Sat}$	$\alpha_{11} = 0.88 = Z_{P@Sat}$
δ Parameters Obtained From $R2$ in $K1 \sim K4$ Clusters			
$K1(R2)$	$K2(R2)$	$K3(R2)$	$K4(R2)$
$\delta_0 = 0.9 = Z_{C@OPBO}$	$\delta_1 = 0.27 = Z_{C@OPBO}$	$\delta_2 = 0.35 = Z_{C@OPBO}$	$\delta_3 = 0.48 = Z_{C@OPBO}$
$\delta_4 = 0.55 = Z_{C@Sat}$	$\delta_5 = 0.63 = Z_{C@Sat}$	$\delta_6 = 0.18 = Z_{C@Sat}$	$\delta_7 = 1 = Z_{C@Sat}$
$\delta_8 = 0.8 = Z_{P@Sat}$	$\delta_9 = 0.4 = Z_{P@Sat}$	$\delta_{10} = 0.33 = Z_{P@Sat}$	$\delta_{11} = 0.11 = Z_{P@Sat}$

parameters for each chosen network, the algorithm must be executed each time.

Next, use the modelled fuzzy logic max operators shown in (15) and (16) to finally obtain the actual load impedances, i.e. (9) and (10) of the carrier and peaking PAs, respectively, as well as the actual characteristic impedance and electrical length for all the transmission lines in each chosen network. Hence, it is through (15) and (16) that the actual DPA impedance and electrical length design values are acquired. Therefore, in order for the proposed theory to be effective in design, the modelled fuzzy logic max operators pertaining to the α and δ parameters can be, respectively, expressed as

$$\sum_{i=1}^{mR1} max(\alpha_0, \alpha_1, ..., \alpha_p) mR1 \tag{15}$$

$$\sum_{j=1}^{nR2} max(\delta_0, \delta_1, ..., \delta_q) nR2. \tag{16}$$

In addition, the fuzzy logic max operators perform the following tasks: (a) make a comparison of the optimal parameters obtained in one region and then select the most suitable and maximum parameter, (b) make a comparison of the optimal parameters obtained across the regions and then finally select the maximum parameter suitable for designing the TW-SDPA and (c) account for the impact of the other parameters on the selected ones. The physical application of (15) and (16) in the acquisition of the load impedances of the carrier and peaking sub-amplifiers are demonstrated as follows. In reference to Table II, it is worth noting that there exist α_0 to α_{11} node parameters relating to $mR1$ in (15). Similarly, there exist δ_0 to δ_{11} node parameters relating to $nR2$ in (16). As a reminder, $mR1$ and $nR2$ designate the total number of selected optimal nodes, i.e. m and n in $R1$ and $R2$, respectively, from $K_1 \sim K_4$ clusters after convergence. Clearly, $mR1$ has 12 α node parameters, i.e. α_0 to α_{11}. Likewise, $nR2$ has 12 δ node parameters, i.e. δ_0 to δ_{11}. From Table II, the selected optimal α values in $R1$ from $K_1 \sim K_4$ clusters are $\alpha_0 = 0.5$,

TABLE III
OPTIMAL α AND δ PARAMETERS OBTAINED FOR Z_n AND θ_n FROM $R1 \sim R2$ IN $K1 \sim K4$ CLUSTERS AFTER CONVERGENCE FOR THE CARRIER-AMPLIFIER OMN AND IIN

α Parameters Obtained From $R1$ in $K1 \sim K4$ Clusters For Carrier-Amplifier OMN Impedance			
$K1(R1)$	$K2(R1)$	$K3(R1)$	$K4(R1)$
$\alpha_0 = 0.01 = Z_9$	$\alpha_1 = 0.029 = Z_9$	$\alpha_2 = 0.1153 = Z_9$	$\alpha_3 = 0.05 = Z_9$
$\alpha_4 = 0.0899 = Z_{10}$	$\alpha_5 = 0.0101 = Z_{10}$	$\alpha_6 = 0.0151 = Z_{10}$	$\alpha_7 = 0.0321 = Z_{10}$
$\alpha_8 = 0.0203 = Z_{11}$	$\alpha_9 = 0.0652 = Z_{11}$	$\alpha_{10} = 0.0978 = Z_{11}$	$\alpha_{11} = 0.0586 = Z_{11}$
α Parameters Obtained From $R1$ in $K1 \sim K4$ Clusters For Carrier-Amplifier OMN Electrical Length			
$K1(R1)$	$K2(R1)$	$K3(R1)$	$K4(R1)$
$\alpha_{12} = 0.02 = \theta_9$	$\alpha_{13} = 0.001 = \theta_9$	$\alpha_{14} = 0.0255 = \theta_9$	$\alpha_{15} = 0.016 = \theta_9$
$\alpha_{16} = 0.07635 = \theta_{10}$	$\alpha_{17} = 0.0111 = \theta_{10}$	$\alpha_{18} = 0.03121 = \theta_{10}$	$\alpha_{19} = 0.05812 = \theta_{10}$
$\alpha_{20} = 0.1105 = \theta_{11}$	$\alpha_{21} = 0.0624 = \theta_{11}$	$\alpha_{22} = 0.0217 = \theta_{11}$	$\alpha_{23} = 0.0913 = \theta_{11}$
δ Parameters Obtained From $R2$ in $K1 \sim K4$ Clusters For Carrier-Amplifier OMN Impedance			
$K1(R2)$	$K2(R2)$	$K3(R2)$	$K4(R2)$
$\delta_0 = 0.04 = Z_9$	$\delta_1 = 0.09 = Z_9$	$\delta_2 = 0.081 = Z_9$	$\delta_3 = 0.053 = Z_9$
$\delta_4 = 0.0589 = Z_{10}$	$\delta_5 = 0.0178 = Z_{10}$	$\delta_6 = 0.07567 = Z_{10}$	$\delta_7 = 0.06565 = Z_{10}$
$\delta_8 = 0.01212 = Z_{11}$	$\delta_9 = 0.1022 = Z_{11}$	$\delta_{10} = 0.0325 = Z_{11}$	$\delta_{11} = 0.2384 = Z_{11}$
δ Parameters Obtained From $R2$ in $K1 \sim K4$ Clusters For Carrier-Amplifier OMN Electrical Length			
$K1(R2)$	$K2(R2)$	$K3(R2)$	$K4(R2)$
$\delta_{12} = 0.0328 = \theta_9$	$\delta_{13} = 0.03 = \theta_9$	$\delta_{14} = 0.005 = \theta_9$	$\delta_{15} = 0.0009 = \theta_9$
$\delta_{16} = 0.04917 = \theta_{10}$	$\delta_{17} = 0.0638 = \theta_{10}$	$\delta_{18} = 0.01958 = \theta_{10}$	$\delta_{19} = 0.0695 = \theta_{10}$
$\delta_{20} = 0.1024 = \theta_{11}$	$\delta_{21} = 0.0964 = \theta_{11}$	$\delta_{22} = 0.1812 = \theta_{11}$	$\delta_{23} = 0.0786 = \theta_{11}$
α Parameters Obtained From $R1$ in $K1 \sim K4$ Clusters For IIN Impedance			
$K1(R1)$	$K2(R1)$	$K3(R1)$	$K4(R1)$
$\alpha_0 = 0.0173 = Z_{37}$	$\alpha_1 = 0.10422 = Z_{37}$	$\alpha_2 = 0.07745 = Z_{37}$	$\alpha_3 = 0.01546 = Z_{37}$
$\alpha_4 = 0.01869 = Z_{38}$	$\alpha_5 = 0.09745 = Z_{38}$	$\alpha_6 = 0.0146 = Z_{38}$	$\alpha_7 = 0.03453 = Z_{38}$
$\alpha_8 = 0.05151 = Z_{39}$	$\alpha_9 = 0.01383 = Z_{39}$	$\alpha_{10} = 0.02235 = Z_{39}$	$\alpha_{11} = 0.03633 = Z_{39}$
α Parameters Obtained From $R1$ in $K1 \sim K4$ Clusters For IIN Electrical Length			
$K1(R1)$	$K2(R1)$	$K3(R1)$	$K4(R1)$
$\alpha_{12} = 0.0469 = \theta_{37}$	$\alpha_{13} = 0.1574 = \theta_{37}$	$\alpha_{14} = 0.06334 = \theta_{37}$	$\alpha_{15} = 0.0197 = \theta_{37}$
$\alpha_{16} = 0.03713 = \theta_{38}$	$\alpha_{17} = 0.02841 = \theta_{38}$	$\alpha_{18} = 0.05479 = \theta_{38}$	$\alpha_{19} = 0.01235 = \theta_{38}$
$\alpha_{20} = 0.04247 = \theta_{39}$	$\alpha_{21} = 0.03986 = \theta_{39}$	$\alpha_{22} = 0.01171 = \theta_{39}$	$\alpha_{23} = 0.02019 = \theta_{39}$
δ Parameters Obtained From $R2$ in $K1 \sim K4$ Clusters For IIN Impedance			
$K1(R2)$	$K2(R2)$	$K3(R2)$	$K4(R2)$
$\delta_0 = 0.01997 = Z_{37}$	$\delta_1 = 0.0451 = Z_{37}$	$\delta_2 = 0.03432 = Z_{37}$	$\delta_3 = 0.0206 = Z_{37}$
$\delta_4 = 0.06107 = Z_{38}$	$\delta_5 = 0.12423 = Z_{38}$	$\delta_6 = 0.0302 = Z_{38}$	$\delta_7 = 0.0783 = Z_{38}$
$\delta_8 = 0.07 = Z_{39}$	$\delta_9 = 0.01584 = Z_{39}$	$\delta_{10} = 0.02509 = Z_{39}$	$\delta_{11} = 0.0791 = Z_{39}$
δ Parameters Obtained From $R2$ in $K1 \sim K4$ Clusters For IIN Electrical Length			
$K1(R2)$	$K2(R2)$	$K3(R2)$	$K4(R2)$
$\delta_{12} = 0.01884 = \theta_{37}$	$\delta_{13} = 0.05707 = \theta_{37}$	$\delta_{14} = 0.08371 = \theta_{37}$	$\delta_{15} = 0.01538 = \theta_{37}$
$\delta_{16} = 0.07138 = \theta_{38}$	$\delta_{17} = 0.01407 = \theta_{38}$	$\delta_{18} = 0.0884 = \theta_{38}$	$\delta_{19} = 0.01121 = \theta_{38}$
$\delta_{20} = 0.01676 = \theta_{39}$	$\delta_{21} = 0.0125 = \theta_{39}$	$\delta_{22} = 0.04521 = \theta_{39}$	$\delta_{23} = 0.05593 = \theta_{39}$

$\alpha_1 = 0.1$, $\alpha_2 = 0.3$ and $\alpha_3 = 0.7$ which are associated to only $Z_{C@OPBO}$. Then, applying (15), these values are expressed as $max(\alpha_0 = 0.5, \alpha_1 = 0.1, \alpha_2 = 0.3, \alpha_3 = 0.7)12$. With the fuzzy logic max operator, the optimal and maximum α value is chosen from the selected α values. That said, 0.7 is chosen and multiplied by $mR1$. For instance, 0.7×12 which becomes 8.4. In that sense, $Z_{C@OPBO}$ is initially set at 8.4 Ω. Similarly, for the selected optimal δ values in $R2$ from $K_1 \sim K_4$ clusters, the following values are selected $\delta_0 = 0.9$, $\delta_1 = 0.27$, $\delta_2 = 0.35$ and $\delta_3 = 0.48$ which are also associated to only $Z_{C@OPBO}$. By applying (16), these values are expressed as $max(\delta_0 = 0.9, \delta_1 = 0.27, \delta_2 = 0.35, \delta_3 = 0.48)12$. Then, the optimal and maximum δ value is chosen from the selected δ values. That said, 0.9 is chosen and multiplied by $nR2$. For example, 0.9×12 which becomes 10.8. In that sense, another value is obtained for $Z_{C@OPBO}$ from $R2$. $Z_{C@OPBO}$ is for the second time set at 10.8 Ω. For the last time, the two values obtained for $Z_{C@OPBO}$ are then subjected to the max operator which then becomes $max(Z_{C@OPBO_0} = 8.4, Z_{C@OPBO_1} = 10.8)24$. For simplicity in the identification of the two $Z_{C@OPBO}$ values obtained, the first parameter is redefined as $Z_{C@OPBO_0}$ while the second is redefined as $Z_{C@OPBO_1}$ as shown. Then, 10.8 is chosen and multiplied by 24. The reason for multiplying by 24 is that in each region, the selected optimal nodes associated to the α and δ parameters are 12. In other words, α has 12 selected optimal nodes in $R1$ and δ has 12 selected optimal nodes in $R2$. Another reason for performing such a task is to factor in the impact of the other parameters on the selected optimal ones. Therefore, adding them gives a total of 24 nodes. The multiplication results in 259.2 Ω. That means, each selected optimal node resulting from δ convergence for $Z_{C@OPBO}$ has the potential of effectively modulating the operation of the carrier amplifier at OPBO. In that sense, for the carrier amplifier to operate effectively at the OPBO level, $Z_{C@OPBO}$ should be set at 10.8 Ω. $Z_{C@Sat} = 12\ \Omega$ and $Z_{P@Sat} = 12\ \Omega$ using the same procedure.

The next step is the acquisition of the suitable characteristic impedance and electrical length of each transmission line in each network of the DPA. To achieve this, Z_n and θ_n where $n = 1, 2, 3, ...$ were introduced in (11) to replace (9) and (10). In obtaining the actual impedance and electrical

TABLE IV
ACTUAL TW-SDPA IMPEDANCE AND ELECTRICAL LENGTH DESIGN VALUES OBTAINED WITH THE PROPOSED TECHNIQUE

Carrier-Amplifier Impedance and Electrical Length Design Values			
IMN	OMN	Gate Biasing Network	Drain Biasing Network
$Z_1 = 50.12\ \Omega\ (\theta_1 = 13.57°)$	$Z_9 = 33.22\ \Omega\ (\theta_9 = 9.45°)$	$Z_{13} = 68.66\ \Omega\ (\theta_{13} = 18.64°)$	$Z_{18} = 68.66\ \Omega\ (\theta_{18} = 3.73°)$
$Z_2 = 25.9\ \Omega\ (\theta_2 = 28.79°)$	$Z_{10} = 25.9\ \Omega\ (\theta_{10} = 21.99°)$	$Z_{14} = 68.66\ \Omega\ (\theta_{14} = 18.64°)$	$Z_{19} = 68.66\ \Omega\ (\theta_{19} = 8.2°)$
$Z_3 = 33.212\ \Omega\ (\theta_3 = 7.87°)$	$Z_{11} = 68.66\ \Omega\ (\theta_{11} = 52.19°)$	$Z_{15} = 68.66\ \Omega\ (\theta_{15} = 18.64°)$	$Z_{20} = 68.66\ \Omega\ (\theta_{20} = 14.54°)$
$Z_4 = 52.17\ \Omega\ (\theta_4 = 24°)$	$Z_{12} = 20.81\ \Omega\ (\theta_{12} = 20.25°)$	$Z_{16} = 68.66\ \Omega\ (\theta_{16} = 7.46°)$	$Z_{21} = 50.12\ \Omega\ (\theta_{21} = 30.58°)$
$Z_5 = 12.18\ \Omega\ (\theta_5 = 48.16°)$	–	$Z_{17} = 50.12\ \Omega\ (\theta_{17} = 30.58°)$	–
$Z_6 = 68.66\ \Omega\ (\theta_6 = 48.46°)$	–	–	–
$Z_7 = 33.22\ \Omega\ (\theta_7 = 15.75°)$	–	–	–
$Z_8 = 6.14\ \Omega\ (\theta_8 = 30.96°)$	–	–	–
Peaking-Amplifier Impedance and Electrical Length Design Values			
IMN	OMN	Gate Biasing Network	Drain Biasing Network
$Z_{22} = 50.12\ \Omega\ (\theta_{22} = 11.47°)$	$Z_{30} = 33.22\ \Omega\ (\theta_{30} = 31.1°)$	$Z_{32} = 68.66\ \Omega\ (\theta_{32} = 18.27°)$	–
$Z_{23} = 33.22\ \Omega\ (\theta_{23} = 7.87°)$	$Z_{31} = 33.22\ \Omega\ (\theta_{31} = 1.97°)$	$Z_{33} = 68.66\ \Omega\ (\theta_{33} = 18.64°)$	–
$Z_{24} = 22.8\ \Omega\ (\theta_{24} = 19.34°)$	–	$Z_{34} = 68.66\ \Omega\ (\theta_{34} = 18.64°)$	–
$Z_{25} = 35.78\ \Omega\ (\theta_{25} = 38.38°)$	–	$Z_{35} = 68.66\ \Omega\ (\theta_{35} = 3.73°)$	–
$Z_{26} = 9.76\ \Omega\ (\theta_{26} = 59.43°)$	–	$Z_{36} = 50.12\ \Omega\ (\theta_{36} = 30.58°)$	–
$Z_{27} = 68.66\ \Omega\ (\theta_{27} = 52.19°)$	–	–	–
$Z_{28} = 19.54\ \Omega\ (\theta_{28} = 12.19°)$	–	–	–
$Z_{29} = 6.42\ \Omega\ (\theta_{29} = 53.38°)$	–	–	–
IIN Impedance and Electrical Length Design Values			
$Z_{37} = 30.02\ \Omega\ (\theta_{37} = 45.33°)$	$Z_{38} = 35.78\ \Omega\ (\theta_{38} = 25.46°)$	$Z_{39} = 22.8\ \Omega\ (\theta_{39} = 16.11°)$	–
PMN Impedance and Electrical Length Design Values			
$Z_{40} = 14.99\ \Omega\ (\theta_{40} = 12.35°)$	$Z_{42} = 22.26\ \Omega\ (\theta_{42} = 47.2°)$	$Z_{44} = 42.36\ \Omega\ (\theta_{44} = 57.29°)$	–
$Z_{41} = 17.42\ \Omega\ (\theta_{41} = 49.04°)$	$Z_{43} = 32.08\ \Omega\ (\theta_{43} = 46.16°)$	$Z_{45} = 50.12\ \Omega\ (\theta_{45} = 30.58°)$	–

Z_n: Impedances of microstrip transmission lines. θ_n: Electrical lengths of microstrip transmission lines. $n = 1, 2, 3, ...$

length values for each network using (15) and (16), the procedure used in acquiring $Z_{C@OPBO}$ is applied. As an example, with reference to Table III, to determine the actual Z_9 and θ_9 shown in Table IV, the selected optimal α and δ values in $R1$ and $R2$ for Z_9 are $\alpha_0 = 0.01, \alpha_1 = 0.03, \alpha_2 = 0.1153, \alpha_3 = 0.05$ and $\delta_0 = 0.04, \delta_1 = 0.09, \delta_2 = 0.081, \delta_3 = 0.053$, respectively. Using (15) and (16), $max(\alpha_0 = 0.01, \alpha_1 = 0.03, \alpha_2 = 0.1153, \alpha_3 = 0.05)12$ and $max(\delta_0 = 0.04, \delta_1 = 0.09, \delta_2 = 0.081, \delta_3 = 0.053)12$, respectively. Then, $0.1153 \times 12 \approx 1.384\ \Omega$ is obtained using (15) while $0.09 \times 12 = 1.08\ \Omega$ is obtained using (16). Next, $max(1.384, 1.08)24$ makes $Z_9 = 1.384 \times 24 \approx 33.22\ \Omega$. Likewise, for θ_9, $\alpha_{12} = 0.02, \alpha_{13} = 0.001, \alpha_{14} = 0.0255, \alpha_{15} = 0.016$ and $\delta_{12} = 0.0328, \delta_{13} = 0.03, \delta_{14} = 0.005, \delta_{15} = 0.0009$. Using (15) and (16), $max(\alpha_{12} = 0.02, \alpha_{13} = 0.001, \alpha_{14} = 0.0255, \alpha_{15} = 0.016)12$ and $max(\delta_{12} = 0.0328, \delta_{13} = 0.03, \delta_{14} = 0.005, \delta_{15} = 0.0009)12$, respectively. Then using (15), $0.0255 \times 12 = 0.306°$ while using (16) $0.0328 \times 12 = 0.3936°$. Next, $max(0.306, 0.3936)24$ makes $\theta_9 = 0.3936 \times 24 \approx 9.45°$. The characteristic impedances and electrical lengths were not strictly bounded. This is because, every node in each cluster possesses possibilities and potentials of donating the right impedance and electrical length to the microstrip lines for bandwidth extension. In the execution of the K-means clustering algorithm, the number of iterations is set to about 14. After the $14th$ iteration, each cluster remained static as well as the obtained α and δ values. This indicates the algorithm has converged and suitable solutions are found.

In summary, one can easily observe that for each α and δ parameter in each region, there exist one $Z_{C@OPBO}$, $Z_{C@Sat}$, $Z_{P@Sat}$, Z_n and θ_n. With (15) and (16), comparisons are made in order to still find the optimal $Z_{C@OPBO}$, $Z_{C@Sat}$, $Z_{P@Sat}$, Z_n and θ_n. In other words, for each $Z_{C@OPBO}$ obtained from the α and δ parameters in each region, (15) and (16) do function to select the optimal $Z_{C@OPBO}$ value suitable for designing the TW-SDPA. Likewise, the same process is carried out for $Z_{C@Sat}$, $Z_{P@Sat}$, Z_n and θ_n in order to find the optimal values. By using (15) and (16), the actual impedance and electrical length design values obtained for the microstrip lines in the IMNs, OMNs, gate and drain biasing networks, IIN and PMN are shown in Table IV. The residue of the design details are given as follows.

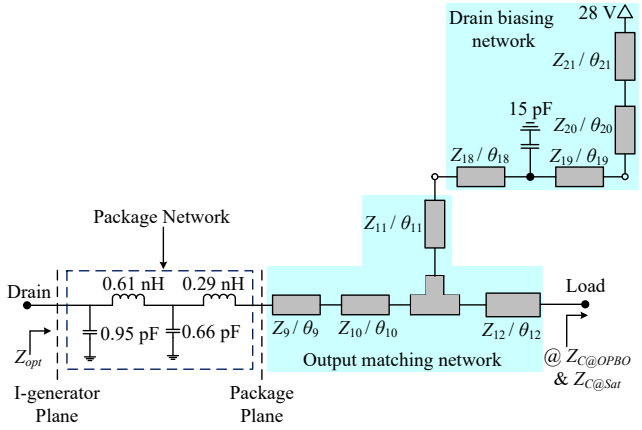

Fig. 6. Carrier device OMN and drain biasing network synthesised at I-generator and package planes

The designed OMN and drain biasing network of the carrier amplifier are displayed in Fig. 6. Moreover, the device package of the CGH40010F transistor is included in the design as shown in the figure. The impedance trajectories of the accomplished carrier device OMN and drain biasing network are demonstrated at OPBO and saturation as shown in Fig. 7. As observed in Fig. 7, the TW-SDPA is capable of providing

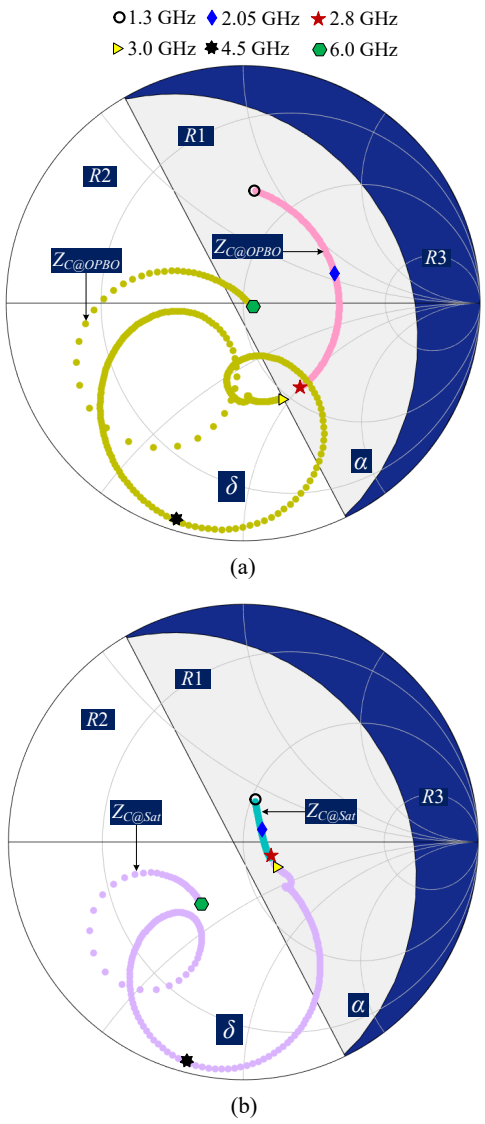

Fig. 7. Load impedance trajectories of carrier device OMN and drian biasing network at (a) OPBO and (b) saturation.

better wideband performance functionalities at OPBO and saturation levels. This demonstration in itself, not only indicates the acquisition of optimal impedance matching solutions at $R1$ and $R2$. Additionally, it also demonstrates the feasibilities of the proposed technique for bandwidth extension in the TW-SDPA. Another more important demonstration not to be overlooked, is the evidence that the impedance trajectories in Z_{CFM1} ($R1$) and Z_{CFM2} ($R2$) as shown in Fig. 7, are within the regions shown in Fig. 3. Therefore, supporting the proof of the design strategy.

Following the separate accomplishments of the carrier and peaking sub-amplifiers, both devices should be put together. A two-section Wilkinson power divider is then designed and positioned at their inputs to combine the carrier and peaking paths.

Finally, Fig. 8 shows the simulated drain efficiency and gain performances of the proposed TW-SDPA. In the 1.3–2.5 GHz operating frequency band, the drain efficiency is within 52.4%–75.3% at saturation and the drain efficiency at 6 dB OPBO is within 43%–55%. The output power is within 42.7–45 dBm while the gain is within 9.7–12 dB at saturation.

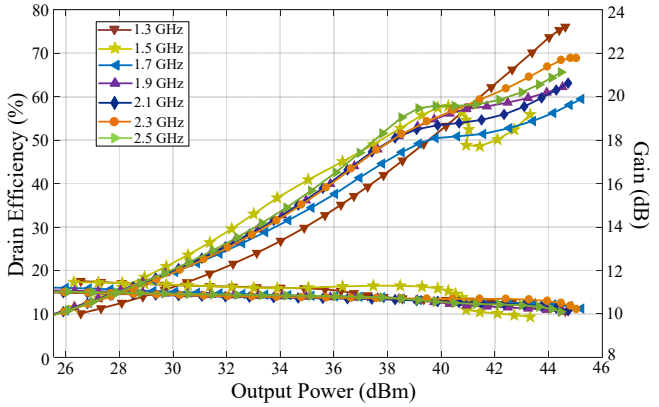

Fig. 8. Simulated drain efficiency and gain performances of the proposed TW-SDPA.

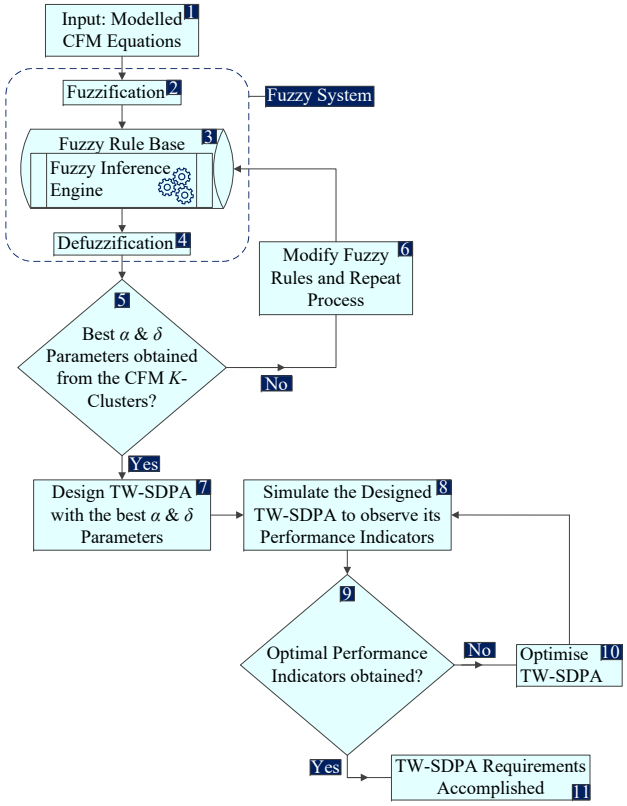

Fig. 9. Proposed CFLMT design flow for TW-SDPAs.

In summary, Fig. 9 shows the flowchart of the procedure used to design TW-SDPAs using the proposed CFLMT.

IV. Experimental Verification

For verification of the proposed design approach, a broadband TW-SDPA was fabricated on a Rogers RO4350B substrate with $\varepsilon_r = 3.66$, $h = 20$ mil and $\delta = 0.003$ as shown in Fig. 10. To evaluate the performance of the designed TW-SDPA, the measurements under continuous wave signals excitations and modulated signals were carried out as demonstrated below.

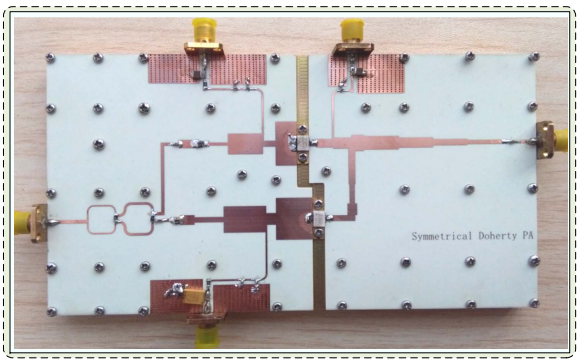

Fig. 10. Photograph of the fabricated TW-SDPA.

A. DPA Measurement Results With Continuous Wave Signals

The proposed TW-SDPA was stimulated by a continuous wave signal sweeping from 1.2 GHz to 2.4 GHz with a step of 0.1 GHz. The TW-SDPA operating frequency band spans from 1.2 GHz to 2.4 GHz, successfully accounting for 66.7% FBW. Fig. 11 shows the measured efficiency and gain as functions of the output power for all the frequency in the band, revealing performances in line with the expectations. Fig. 12 shows the comparison between measured and simulated drain efficiencies at 6 dB OPBO and saturation. The experimental results clearly indicate that at saturation and 6 dB OPBO, 41.59%–81.1% and 35%–63% drain efficiencies are, respectively, achieved

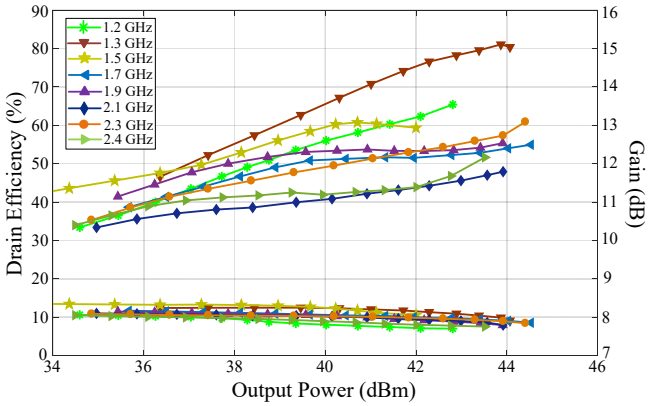

Fig. 11. Measured drain efficiency and gain performances of the proposed TW-SDPA.

successfully in the 1.2–2.4 GHz working band. The working band of the proposed TW-SDPA indicates 15.5%–29.7% increment in FBW when compared with the continuous mode-based TW-SDPAs reported by Chen *et al.* [32–34] and Shi *et al.* [35–36]. Fig. 13 shows the measured and simulated output power of the proposed TW-SDPA at 6 dB OPBO and saturation. At saturation, 42–45 dBm output power is achieved while at 6 dB OPBO, 35.52–39 dBm output power is recorded in measurement.

B. DPA Measurement Results With Modulated Signals

To evaluate the capability of the fabricated TW-SDPA to efficiently work in wireless communication systems, it was tested with a 20-MHz long-term evolution (LTE) modulated signal characterised by a peak-to-average power ratio (PAPR)

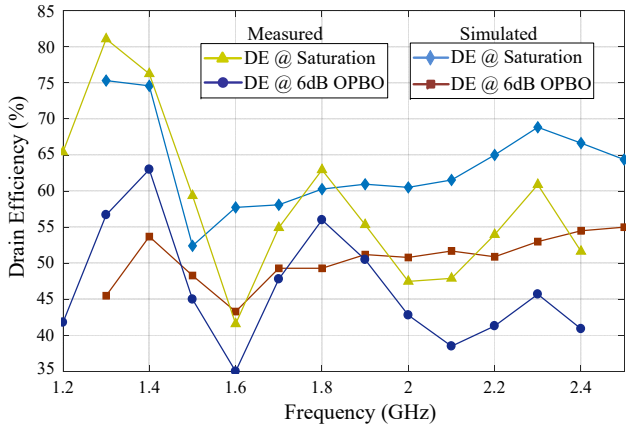

Fig. 12. Measured and simulated drain efficiencies of the proposed TW-SDPA at OPBO and saturation.

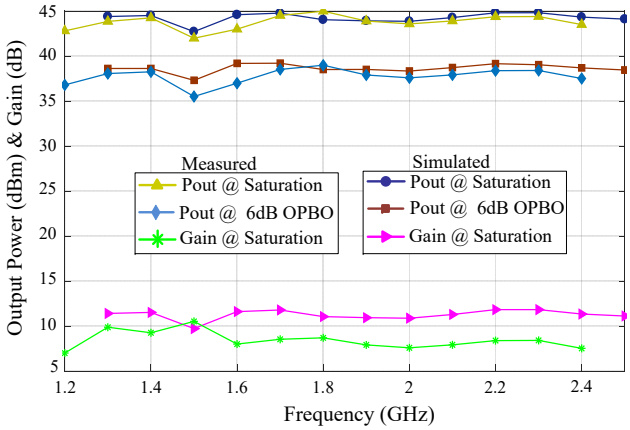

Fig. 13. Measured and simulated output power (Pout) and gain of the proposed TW-SDPA.

of 8 dB. In these measurements, the modulated signal is generated by a vector signal generator while the output spectrum and adjacent channel leakage ratio (ACLR) are measured by a vector signal analyzer. Indirect learning approach is used to realise a DPD function also. In particular, a memory polynomial model with nonlinear order 4 and memory depth 13 is chosen to build the DPD structure. All the model parameters are estimated through the least square algorithm. As a proof of the effectiveness of the DPD, Fig. 14 shows the captured DPA spectra at 2.3 GHz and in correspondence of an average output power of 36.7 dBm before and after DPD. In the latter case, the ACLR is reduced from –28 dBc to –47 dBc. For completeness, Fig. 15 summarises the measured ACLR before and after DPD, the average output power (Pout) (36–37 dBm) and drain efficiency (DE) (higher than 46%) when the TW-SDPA is driven with the same modulated signal in the overall working frequency band, i.e. 1.2–2.4 GHz, step 0.1 GHz. Notably, similar levels of linearity improvements have been registered.

A summary of performance comparison of this work with some recently reported TW-SDPAs is presented in Table V. Table V suggests the efficacy of the proposed design approach and thus showing its wide FBW performance achieved with comparable results.

TABLE V
COMPARISON WITH SOME RECENTLY REPORTED TWO-WAY GAN SYMMETRICAL DOHERTY POWER AMPLIFIERS

Reference	Frequency (GHz)	FBW (GHz) (%)	Output Power (dBm)	Gain (dB)	η_{sat} (%)	η_{6dB} (%)	Proposed Technique
[29]	1.7–2.6	0.9 (42)	44.6–46.3	8.6–10.5	57–66	47–57	Post-Matching
[30]	1.5–2.5	1.0 (50)	42–44.5	8–11	55–75	42–53	Novel Combiner
[31]	1.5–2.4	0.9 (46)	43.1–44.4	Not indicated	57–74	45–56	Bayesian Optimisation
[32]	1.7–2.7	1.0 (45.5)	52.7–54.3*	12.3–13.7	53–66	40–50.2	Continuous Mode
[33]	1.65–2.75	1.1 (50)	44–46	7–8	60–75	50–60	Continuous Mode
[34]	1.65–2.75	1.1 (50)	44.5–46.3	9.3–11.7	60–77	52–66	Continuous Mode
[35]	1.6–2.7	1.1 (51)	43.8–45.2	9.4–11.5	56–75.3	46.5–63.5	Continuous Mode
[36]	1.65–2.4	0.75 (37)	43.5–45.1	11.5–12.1	60.1–76.2	46–57	Continuous Mode
[37]	1.5–2.6	1.1 (53.6)	41.8	>9	40–45	31–35	Klopfenstein Taper
[40]	1.05–2.55	1.5 (83.3)	40–42	>7	45–83	35–58	Closed-Form
[42]	1.1–2.4	1.3 (74)	43.3–45.4	9.5–11.1	55.4–68	43.8–54.9	Complex Combining Load
[43]	1.5–3.8	2.3 (87)	42.3–43.4	10–13.8	42–63	33–55	Bandwidth Estimation
This Work	1.2–2.4	1.2 (66.7)	42–45	7–10.52	41.59–81.1	35–63	Continuous Fuzzy Logic Mode

FBW: Fractional bandwidth. η_{sat}: Drain efficiency at saturation. η_{6dB}: Drain efficiency at 6 dB output-power-back-off level.
*: Used two 100 W GaN HEMTs CGHV40100 in design.

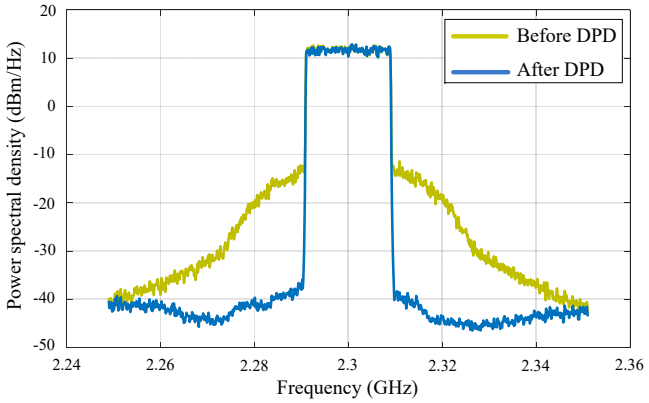

Fig. 14. Measured normalised power spectral density with 20-MHz LTE signal and PAPR of 8 dB at 2.3 GHz before and after DPD.

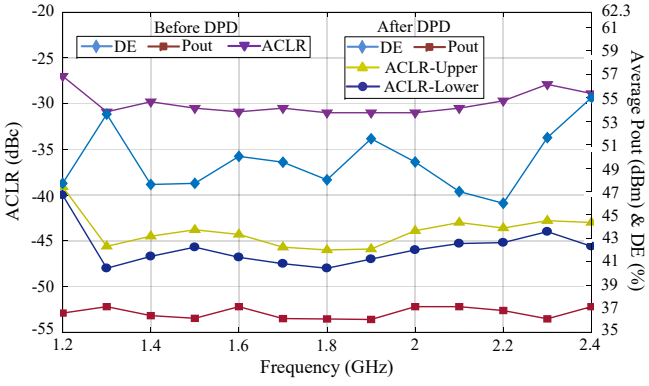

Fig. 15. Measured ACLR, average output power (Pout) and drain efficiency (DE) across 1.2–2.4 GHz working frequency band.

V. CONCLUSION

This paper introduced a continuous fuzzy logic mode technique for bandwidth extension in continuous mode-based TW-SDPAs. The proposed technique uses a modelled K-means unsupervised learning clustering algorithm and continuous mode technique in a modelled fuzzy logic system environment. A TW-SDPA was designed and fabricated to validate the proposed theory. The experimental results with continuous wave signals excitations clearly demonstrated that the TW-SDPA achieved drain efficiencies within 41.59%–81.1% and 35%–63% at saturation and 6 dB OPBO levels, respectively, 42–45 dBm output power and 7–10.52 dB gain over a frequency range spanning from 1.2 GHz to 2.4 GHz. Correspondingly, a FBW of 66.7% was successfully achieved. Upon comparing the obtained FBW in this work to that of the reported continuous mode-based TW-SDPAs in the literature, the proposed TW-SDPA successfully achieved 15.5%–29.7% increment in FBW. Furthermore, the performance assessment under modulated signals confirmed ACLR better than –46 dBc and average drain efficiency within 46%–55% was successfully obtained. According to the recorded experimental results, it is worth mentioning that this technique showed excellent resiliency to the FBW inaccuracies of existing continuous mode-based TW-SDPAs.

REFERENCES

[1] M. Stoopman, K. Philips, and W. A. Serdijn, "An RF-powered DLL-based 2.4-GHz transmitter for autonomous wireless sensor nodes," *IEEE Trans. Microw. Theory and Techn.*, vol. 65, no. 7, pp. 2399–2408, July 2017.
[2] T. Qi and S. He, "Further efficiency improvement of power amplifiers using thermal energy harvesting," *IEEE Trans. Ind. Electron.*, vol. 66, no. 12, pp. 9628–9631, Dec. 2019.

[3] S. Yang, J. Yin, H. Yi, W. Yu, P. Mak, and R. P. Martins, "A 0.2-V energy-harvesting BLE transmitter with a micropower manager achieving 25% system efficiency at 0-dBm Output and 5.2-nW sleep power in 28-nm CMOS," *IEEE J. Solid-State Circuits*, vol. 54, no. 5, pp. 1351–1362, May 2019.

[4] G. A. F. de Souza, R. B. dos Santos, and L. de Abreu Faria, "Low-power current-mode interval type-2 fuzzy inference engine circuit," *IEEE Trans. Circuits Syst. I, Reg. Papers*, vol. 66, no. 7, pp. 2639–2650, July 2019.

[5] H. Han, L. Zhang, X. Wu, and J. Qiao, "An efficient second-order algorithm for self-organizing fuzzy neural networks," *IEEE Trans. Cybern.*, vol. 49, no. 1, pp. 14–26, Jan. 2019.

[6] M. Isaksson, D. Wisell, and D. Ronnow, "Wide-band dynamic modeling of power amplifiers using radial-basis function neural networks," *IEEE Trans. Microw. Theory Techn.*, vol. 53, no. 11, pp. 3422–3428, Nov. 2005.

[7] J. Zhai, J. Zhou, L. Zhang, J. Zhao, and W. Hong, "Dynamic behavioral modeling of power amplifiers using ANFIS-based hammerstein," *IEEE Microw. Wireless Compon. Lett.*, vol. 18, no. 10, pp. 704–706, Oct. 2008.

[8] J. Zhai, J. Zhou, L. Zhang, J. Zhao, and W. Hong, "The dynamic behavioral model of RF power amplifiers with the modified ANFIS," *IEEE Trans. Microw. Theory Techn.*, vol. 57, no. 1, pp. 27–35, Jan. 2009.

[9] J. Zhai, J. Zhou, L. Zhang, and W. Hong, "Behavioral modeling of power amplifiers with dynamic fuzzy neural networks," *IEEE Microw. Wireless Compon. Lett.*, vol. 20, no. 9, pp. 528–530, Sept. 2010.

[10] S. Jain, "Analysis and simulation of electrical parameters of fuzzy system using different types of current amplifiers with different membership functions for AkT pathway," in *Fourth Int. Conf. Image Inf. Process.*, Dec. 2017, pp. 1–5.

[11] V. P. G. Jimenez, Y. Jabrane, A. G. Armada, B. Ait Es Said, and A. Ait Ouahman, "High power amplifier pre-distorter based on neural-fuzzy systems for OFDM signals," *IEEE Trans. Broadcast.*, vol. 57, no. 1, pp. 149–158, March. 2011.

[12] K. C. Lee and P. Gardner, "Adaptive neuro-fuzzy inference system (ANFIS) digital predistorter for RF power amplifier linearization," *IEEE Trans. Veh. Techn.*, vol. 55, no. 1, pp. 43–51, Jan. 2006.

[13] J. C. Nunez-Perez *et al.*, "FPGA realization of RF-PA models with memory effects based on ANFIS," in *IEEE Int. Autumn Meeting Power, Electron. Comput.*, Nov. 2016, pp. 1–6.

[14] M. J. Rezaei, A. A. Shahraki, and S. B. Shokouhi, "A review of intelligent predistortion methods for the linearization of RF power amplifiers," in *Int. Conf. Comput. Appl. Techn.*, Jan. 2013, pp. 1–6.

[15] A. Grebennikov and J. Wong, "A dual-band parallel Doherty power amplifier for wireless applications," *IEEE Trans. Microw. Theory Techn.*, vol. 60, no. 10, pp. 3214–3222, Oct. 2012.

[16] A. Gupta and R. K. Jha, "A survey of 5G network: architecture and emerging technologies," *IEEE Access*, vol. 3, no. , pp. 1206–1232, 2015.

[17] M. Akbarpour, M. Helaoui, and F. M. Ghannouchi, "A transformer-less load-modulated (TLLM) architecture for efficient wideband power amplifiers," *IEEE Trans. Microw. Theory Techn.*, vol. 60, no. 9, pp. 2863–2874, Sept. 2012.

[18] S. Chen and Q. Xue, "Optimized load modulation network for Doherty power amplifier performance enhancement," *IEEE Trans. Microw. Theory Techn.*, vol. 60, no. 11, pp. 3474–3481, Nov. 2012.

[19] D. Gustafsson, C. M. Andersson, and C. Fager, "A modified Doherty power amplifier with extended bandwidth and reconfigurable efficiency," *IEEE Trans. Microw. Theory Techn.*, vol. 61, no. 1, pp. 533–542, Jan. 2013.

[20] P. Saad, P. Colantonio, L. Piazzon, F. Giannini, K. Andersson, and C. Fager, "Design of a concurrent dual-band 1.8-2.4 GHz GaN-HEMT Doherty power amplifier," *IEEE Trans. Microw. Theory Techn.*, vol. 60, no. 6, pp. 1840–1849, June 2012.

[21] G. Sun and R. H. Jansen, "Broadband Doherty power amplifier via real frequency technique," *IEEE Trans. Microw. Theory Techn.*, vol. 60, no. 1, pp. 99–111, Jan. 2012.

[22] D. Y. T. Wu and S. Boumaiza, "A modified Doherty configuration for broadband amplification using symmetrical devices," *IEEE Trans. Microw. Theory Techn.*, vol. 60, no. 10, pp. 3201–3213, Oct. 2012.

[23] X. A. Nghiem, J. Guan, T. Hone, and R. Negra, "Design of concurrent multiband Doherty power amplifiers for wireless applications," *IEEE Trans. Microw. Theory Techn.*, vol. 61, no. 12, pp. 4559–4568, Dec. 2013.

[24] X. H. Fang and K. K. M. Cheng, "Extension of high-efficiency range of Doherty amplifier by using complex combining load," *IEEE Trans. Microw. Theory Techn.*, vol. 62, no. 9, pp. 2038–2047, Sept. 2014.

[25] S. Hu, S. Kousai, and H. Wang, "Antenna impedance variation compensation by exploiting a digital Doherty power amplifier architecture," *IEEE Trans. Microw. Theory Techn.*, vol. 63, no. 2, pp. 580–597, Feb. 2015.

[26] X.A. Nghiem, J. Guan, T. Hone, and R. Negra, "Broadband sequential power amplifier with Doherty-type active load modulation," *IEEE Trans. Microw. Theory Techn.*, vol. 63, no. 9, pp. 2821–2832, Sept. 2015.

[27] J. Xia, M. Yang, Y. Guo, and A. Zhu, "A broadband high-efficiency Doherty power amplifier with integrated compensating reactance," *IEEE Trans. Microw. Theory Techn.*, vol. 64, no. 7, pp. 2014–2024, July 2016.

[28] R. Darraji, F. M. Ghannouchi, and M. Helaoui, "Mitigation of bandwidth limitation in wireless Doherty amplifiers with substantial bandwidth enhancement using digital techniques," *IEEE Trans. Microw. Theory Techn.*, vol. 60, no. 9, pp. 2875–2885, Sept. 2012.

[29] J. Pang, S. He, C. Huang, Z. Dai, J. Peng, and F. You, "A post-matching Doherty power amplifier employing low-order impedance inverters for broadband applications," *IEEE Trans. Microw. Theory Techn.*, vol. 63, no. 12, pp. 4061–4071, Dec. 2015.

[30] S. Chen, G. Wang, Z. Cheng, and Q. Xue, "A bandwidth enhanced Doherty power amplifier with a compact output combiner," *IEEE Microw. Wireless Compon. Lett.*, vol. 26, no. 6, pp. 434–436, Jun. 2016.

[31] P. Chen, J. Xia, B. M. Merrick, and T. J. Brazil, "Multiobjective Bayesian optimization for active load modulation in a broadband 20-W GaN Doherty power amplifier design," *IEEE Trans. Microw. Theory Techn.*, vol. 65, no. 3, pp. 860–871, March 2017.

[32] X. Chen, W. Chen, Q. Zhang, F. M. Ghannouchi, and Z. Feng, "A 200 watt broadband continuous-mode doherty power amplifier for base-station applications," in *IEEE MTT-S Int. Microw. Symp. Dig.*, June 2017, pp. 1110–1113.

[33] X. Chen, W. Chen, F. M. Ghannouchi, and Z. Feng, "A 1.1 GHz bandwidth, 46%-62% efficiency continuous mode Doherty power amplifier," in *IEEE MTT-S Int. Microw. Symp. Dig*, May 2016, pp. 1–4.

[34] X. Chen, W. Chen, F. M. Ghannouchi, Z. Feng, and Y. Liu, "A broadband Doherty power amplifier based on continuous-mode technology," *IEEE Trans. Microw. Theory Techn.*, vol. 64, no. 12, pp. 4505–4517, Dec. 2016.

[35] W. Shi *et al.*, "Broadband continuous-mode Doherty power amplifiers with noninfinity peaking impedance," *IEEE Trans. Microw. Theory Techn.*, vol. 66, no. 2, pp. 1034–1046, Feb. 2018.

[36] W. Shi, S. He, and Q.-an Liu, "Design of broadband highly efficient Doherty power amplifiers by using series of continuous modes," in *IEEE MTT-S Int. Microw. Symp. Dig*, May 2016, pp. 1–4.

[37] M.S. Khan *et al.*, "A novel two-stage broadband Doherty power amplifier for wireless applications," *IEEE Microw. Wireless Compon. Lett.*, vol. 28, no. 1, pp. 40–42, Jan. 2018.

[38] J.M. Rubio, J. Fang, V. Camarchia, R. Quaglia, M. Pirola, and G. Ghione, "3-3.6 GHz wideband GaN Doherty power amplifier exploiting output compensation stages," *IEEE Trans. Microw. Theory Techn.*, vol. 60, no. 8, pp. 2543–2548, Aug. 2012.

[39] R. Giofrè, L. Piazzon, P. Colantonio, and F. Giannini, "A Doherty architecture with high feasibility and defined bandwidth behavior," *IEEE Trans. Microw. Theory Techn.*, vol. 61, no. 9, pp. 3308–3317, Sept. 2013.

[40] R. Giofrè, L. Piazzon, P. Colantonio, and F. Giannini, "A closed-form design technique for ultra-wideband Doherty power amplifiers," *IEEE Trans. Microw. Theory Techn.*, vol. 62, no. 12, pp. 3414–3424, Dec. 2014.

[41] R. Giofrè, P. Colantonio, F. Giannini, and L. Piazzon, "New output combiner for Doherty amplifiers," *IEEE Microw. Wireless Compon. Lett.*, vol. 23, no. 1, pp. 31–33, Jan. 2013.

[42] Z. Yang *et al.*, "Bandwidth extension of Doherty power amplifier using complex combining load with noninfinity peaking impedance," *IEEE Trans. Microw. Theory Techn.*, vol. 67, no. 2, pp. 765–777, Feb. 2019.

[43] J. J. M. Rubio, V. Camarchia, M. Pirola, and R. Quaglia, "Design of an 87% fractional bandwidth Doherty power amplifier supported by a simplified bandwidth estimation method," *IEEE Trans. Microw. Theory Techn.*, vol. 66, no. 3, pp. 1319–1327, March 2018.

[44] V. Camarchia, M. Pirola, R. Quaglia, S. Jee, Y. Cho, and B. Kim, "The Doherty power amplifier: review of recent solutions and trends," *IEEE Trans. Microw. Theory Techn.*, vol. 63, no. 2, pp. 559–571, Feb. 2015.

[45] J. Xia, X. Zhu, L. Zhang, J. Zhai, and Y. Sun, "High-efficiency GaN Doherty power amplifier for 100-MHz LTE-Advanced application based on modified load modulation network," *IEEE Trans. Microw. Theory Techn.*, vol. 61, no. 8, pp. 2911–2921, Aug. 2013.

[46] J. Chen, S. He, F. You, R. Tong, and R. Peng, "Design of broadband high-efficiency power amplifiers based on a series of continuous modes," *IEEE Microw. Wireless Compon. Lett.*, vol. 24, no. 9, pp. 631–633, Sept. 2014.

[47] L. A. Zadeh, "Fuzzy sets," *Information and Control*, vol. 8, pp. 338–353, 1965.

[48] R. M. Fano, "Theoretical limitations on the broadband matching of arbitrary impedances," *J. Franklin Inst.*, vol. 249, pp. 57–83, Jan. 1950.